RESEARCH ARTICLE

National Science Open
1: 20220020, 2022
https://doi.org/10.1360/nso/20220020

Information Sciences

Special Topic: Novel Optoelectronic Devices

Direct laser writing of graphene oxide for ultra-low power consumption memristors in reservoir computing for digital recognition

Min Chen[1,2], Zhengfen Wan[1,2], Hao Dong[1,2], Qinyu Chen[1,2], Min Gu[1,2,*] & Qiming Zhang[1,2,*]

[1]*Institute of Photonic Chips, University of Shanghai for Science and Technology, Shanghai 200090, China;*
[2]*Centre for Artificial-Intelligence Nanophotonics, School of Optical-Electrical and Computer Engineering, University of Shanghai for Science and Technology, Shanghai 200090, China*

*Corresponding authors (emails: qimingzhang@usst.edu.cn (Min Gu); gumin@usst.edu.cn (Qiming Zhang))

Received 10 March 2022; Revised 12 April 2022; Accepted 12 May 2022; Published online 10 August 2022

Abstract: A memristor is a promising candidate of new electronic synaptic devices for neuromorphic computing. However, conventional memristors often exhibit complex device structures, cumbersome manufacturing processes, and high energy consumption. Graphene-based materials show great potential as the building materials of memristors. With direct laser writing technology, this paper proposes a lateral memristor with reduced graphene oxide (rGO) and Pt as electrodes and graphene oxide (GO) as function material. This Pt/GO/rGO memristor with a facile lateral structure can be easily fabricated and demonstrates an ultra-low energy consumption of 200 nW. Typical synaptic behaviors are successfully emulated. Meanwhile, the Pt/GO/rGO memristor array is applied in the reservoir computing network, performing the digital recognition with a high accuracy of 95.74%. This work provides a simple and low-cost preparation method for the massive production of artificial synapses with low energy consumption, which will greatly facilitate the development of neural network computing hardware platforms.

Keywords: direct laser writing, memristor array, graphene oxide, reservoir computing

INTRODUCTION

Current computers in use are mostly designed based on the von Neumann architecture that physically separates the central processing unit (CPU) and the memory, thus resulting in sequential instruction processing, and limited throughput. Due to the von Neumann bottleneck, the throughput rate of the CPU is greatly restricted and a “storage wall” is formed over time [1]. Therefore, computational efficiency and power consumption have become very significant problems in the field of artificial intelligence (AI), which always requires enormous and multi-tasking data-processing. To solve this problem, scientists have proposed neuromorphic computing (NC) [2], a hardware system that can parallelly perform storage and computing, simulating the neurobiological structure of the nervous system. Electronic devices with the characteristics of biological synapses and neurons are an essential part of the realization of NC [3]. Memristors have drawn great attention to its nonlinear resistance, which can be modulated with the input voltage and current [4].

© The Author(s) 2022. Published by China Science Publishing & Media Ltd. and EDP Sciences. This is an Open Access article distributed under the terms of the Creative Commons Attribution License (https://creativecommons.org/licenses/by/4.0), which permits unrestricted use, distribution, and reproduction in any medium, provided the original work is properly cited.

More importantly, memristors have demonstrated the potential application for artificial synapses [5–7] and neurons [8] in NC hardware [9] due to the remarkable data processing capabilities [10].

In 2008, Strukov *et al.* [11] first manufactured memristive physical devices with the Pt/TiO_2/Pt structure. Conventional memristors were metal-insulator-metal (MIM)-structured two-terminal devices [12]. Metals (Al [13], Cu [14], Au [15], Ag [16], etc.) are often applied as electrode layer of the memristor and the active layer of memristor is usually made of metal oxides (HfO_2 [17], TaO_x [18], Al_2O_3 [19], TiO_2 [20], etc.). However, memristors with pure metal electrode structure or metal oxide active layer structure require a large forming voltage [21] and generate a large turn-on current [22], which results in high power consumption and greatly limits the integration and practical application. Moreover, traditional metal electrode materials are rigid and cannot meet the development requirements of modern electronic technology such as flexibility, wear resistance and stretchability [23]. Graphene is a two-dimensional (2D) material with a thickness of only one carbon atom layer with excellent properties such as ultra-high mobility, ultra-high thermal conductivity, and transparency [24]. Due to their interesting physical and chemical properties, they have become one of the most promising candidate materials for memristors [25]. Direct laser writing (DLW) technology is a kind of micro/nano processing method without mask, widely applicable, and cost-effective [26]. Graphene oxide (GO) is widely and effectively used in the preparation of graphene due to its strong compatibility, easy regulation, and large-scale production [27]. Reduced graphene oxide (rGO) can be fabricated by photo-thermal and photochemical reduction of GO, and the oxygen-containing functional groups attached to the surface of GO can be effectively removed [28]. The properties similar to graphene make rGO an ideal material that can be widely used in biological sensors [29], generators [30] or storage devices [31]. The efficient fabrication method of laser processing made large-scale processing of graphene-based memristive devices possible [32]. However, DLW is only used for the electrode fabrication of a single device. The fabrication of memristor arrays for neural network hardware which is an essential step to build NC hardware is not involved.

Herein, we report the lateral structure memristor based on Pt/GO/rGO, which presents a stable synaptic learning characteristic with ultra-low energy consumption (200 nW) and good uniformity. With DLW based on femtosecond (fs) laser, GO was reduced to rGO as an electrode and Pt was used as another electrode. As a novel 2D material, rGO possesses high crystallinity, high flexibility, great flexibility and mechanical durability. Using rGO as one electrode of the memristor can overcome the rigidity of the metal electrode, and it is expected to realize the all-carbon-based memristor, which can better realize the large-scale integration of the memristor and be compatible with more graphene-based electronic components. GO is employed as an active layer to make a dynamic memristor that can be repeatedly erased and written. The lateral structure of the memristor exhibits a greatly simple fabrication process compared to the vertical structure [33] and DLW for memristor array further realizes high precision, simple and efficient integrated machining method. It may provide a low-cost and high-efficiency manufacturing process for the practical application of various electronic devices based on rGO. Furthermore, we applied the 5×1 memristive array to reservoir computing (RC) system for digital recognition with an accuracy of 95.74%. Our results open a way of low-cost, fast and simple DLW manufacturing process and the application of micro-nano-size memristive devices in neural networks.

RESULTS AND DISCUSSION

Figure 1A shows a schematic diagram of the memristors enabled by DLW, where Pt and rGO are used as two electrodes of the device and GO is sandwiched between two electrodes as the active layer. An 869 nm thick GO film (Figure S1, Supporting Information) was prepared on a fused silica substrate by drop-cast method. The GO films prepared by drip can be transferred to flexible substrates for the integration of flexible devices. Then a 50 nm thick Pt electrode was prepared on the GO film by magnetron sputtering (see Experimental Section). The other electrode is obtained by photoreduction of GO into rGO by a DLW system with an fs laser (780 nm wavelength, 80 MHz repetition rate). The width of the GO region between two electrodes is 60 μm (Figure S2, Supporting Information). Figure 1B shows an optical image of the device under an optical microscope. DLW is a low-cost, time-saving and mask-less manufacturing process, which can simultaneously realize the direct formation and patterning of rGO. The synapse is the part of the brain where the axons of the anterior neurons and the dendrites of the posterior neurons are connected. The synapse structure is shown in Figure 1C. The plasticity of synapses is the basis for the brain to realize important functions such as learning and memory. The lateral structure of Pt/GO/rGO memristors has dynamic characteristic changes under pulse stimulation to achieve short-term potentiation (STP) and short-term depression (STD). As shown in Figure 1D, the conductance of the device can be gradually increased under 5 consecutive pulses (5 V, 500 μs). Under the continuous reverse stimuli, the conductance can be decreased continuously. This feature emulates the STP/STD of synapse, which is a key function of the biological synapses to realize learning and memory.

To ensure that the GO film is well reduced while not being ablated by a high-power laser, we have studied the influence of laser power on the degree of reduction of GO. When the laser irradiates the GO surface, the

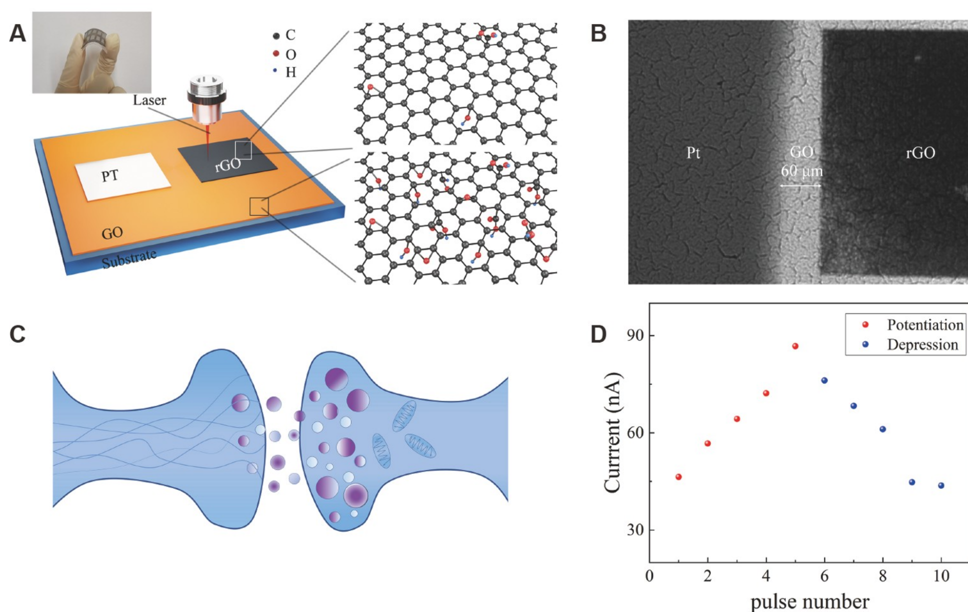

Figure 1 (A) Schematic drawing of Pt/GO/rGO memristor structure enabled by direction laser writing; (B) an optical image of the Pt/GO/rGO memristor captured by an optical microscope; (C) schematic image of the synapse stracture; (D) the synaptic potentiation and depression under the modulation of cyclic pulse signals.

photothermal and photochemical effect triggered by the laser will remove oxygen-containing functional groups and increase the percentage of carbon atoms and restore the sp^2 hybrid C–C bond [34]. The laser power can be adjusted to achieve different degrees of reduction to modulate the conductivity of the sample. As shown in Figure 2, the morphology and chemical structure of GO were studied under irradiation with different laser powers to avoid high-power laser ablation. Figure 2A shows the scanning electron microscope (SEM) image of GO surface and rGO enabled by fs DLW with a laser power of 16 mW, with a spot size of 1.9 μm diameter. The laser-treated GO film shows a rough surface with high porosity, which is caused by the rapid release of gas produced by the removal of oxygen-containing functional groups during the laser reduction process. The color of rGO under the optical microscope is also significantly different after DLW (Figure S3, Supporting Information).

After photoreduction process, the depression on the surface of the film can be clearly seen from the atomic force microscope (AFM) image (Figure 2B). On the surface, the surface sinking after laser irradiation may be caused by an effect called laser shock hardening in which shock waves due to the momentum transfer of photons to photon-absorbing atoms recombine atoms in the material [35]. Here, the fs laser beam directly irradiates and interacts with the GO film, resulting in the removal of oxygen-containing functional groups in GO [36]. In addition, the point-like topography of the laser acting on the surface of GO was observed by SEM and an obvious laser ablation could be seen (Figure S4, Supporting Information). Therefore, here the rGO surface depression should be due to the mass loss caused by laser ablation [37] and the rearrangement of atoms. Raman spectroscopy provides an effective way to distinguish GO and rGO by crystal structure information. The Raman spectra of the GO sample and rGO sample are composed of three characteristic bands at approximately 1355 (D), 1620 (G), and 2700 cm^{-1} (2D) in Figure 2C. The change of defects is mainly characterized by the relative intensity, I_D/I_G ratio, and the intensity of 2D-band [38]. Therefore, Figure 2C shows the evolution of defects and the change of layer structure in GO samples with the increase of

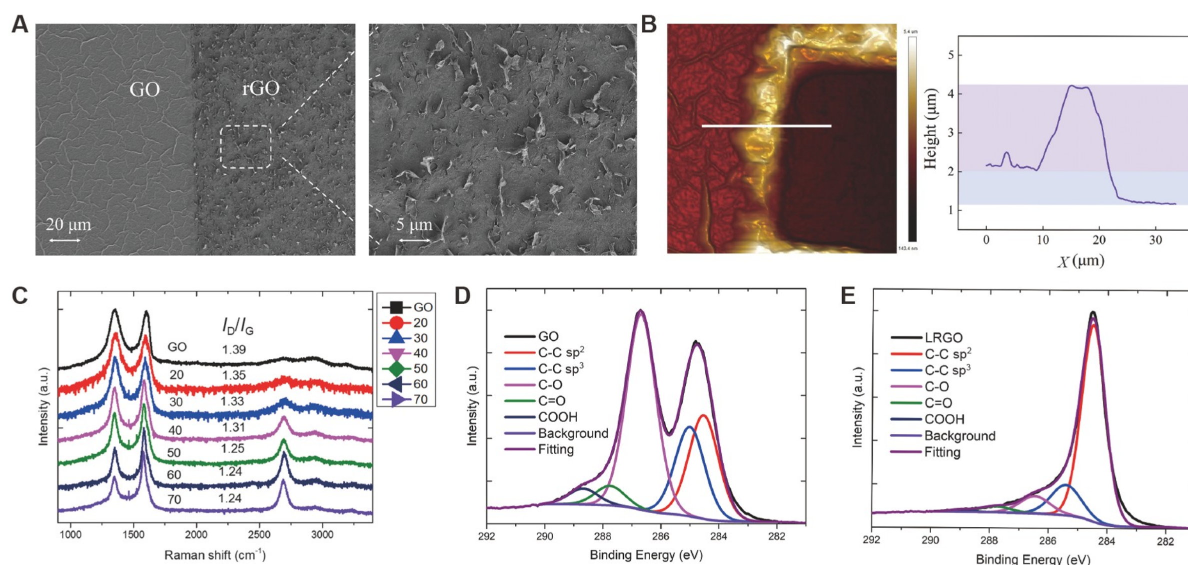

Figure 2 Structural characterization of GO and rGO. (A) SEM image of GO and rGO enabled by DLW at a laser power of 16 mW; (B) an AFM image and line profile of rGO and GO edges; (C) Raman spectra obtained from the GO film before and after the laser reduction for different laser powers; (D) the C 1s peak from the XPS spectrum of the GO sample; (E) the C 1s peak from the XPS spectrum of the rGO sample.

laser power percentage. With the increase of laser power, D and G bands narrow, I_D/I_G ratio decreases, and the number of defects decreases. At the same time, the 2D-band representing the graphite state gradually increases. The structural changes of GO films irradiated by laser were reflected by X-ray photoelectron spectroscopy (XPS) [39]. Comparing the carbon to oxygen ratio (C/O) between GO and rGO provides an effective measurement of the degree of reduction achieved using a simple low-energy infrared laser. It can be observed that the initial percentages of C–C and C–O in GO are 44.75% and 55.25%, respectively (Figure 2D). After laser reduction, the fractional ratio C–C and C–O in GO became 86.79% and 13.21%, respectively (Figure 2E). The C–O and C=O bonds in GO can be broken by laser. Laser treatment converts most of the sp^3 carbon into sp^2 hybrid carbon, leading to the reduction of GO.

Figure 3 shows the electrical characteristics of the device. The initial feature of Pt/GO/rGO memristor is to cyclically apply a triangular voltage bias [5, −5] V on the two surface electrodes, while monitoring the driving current through a Keithley 4200 semiconductor parameter analyzers in Figure 3A. It can be seen that the device has the distinct characteristics of a bipolar memristor. Under the direct current (DC) sweep bias, the *I*-*V* curve of the device shows the typical hysteresis loop of the memristor. As shown in Figure 3A, the device presents two resistance states. When the positive bias voltage is applied to the device, the resistance state of the device is a high resistance state (HRS). When the positive voltage threshold is reached, the resistance state of the device changes from HRS to low resistance state (LRS), which is called SET. RESET refers to the process that the device changes from LRS to HRS again when the negative bias applied to the electrode reaches the threshold. The conductivity of the device is changed by switching between positive and negative threshold voltages, indicating the presence of bipolar resistance switching behavior. The *I*-*V* characteristics also show asymmetric characteristics due to carrier transport caused by the interfacial barrier [40].

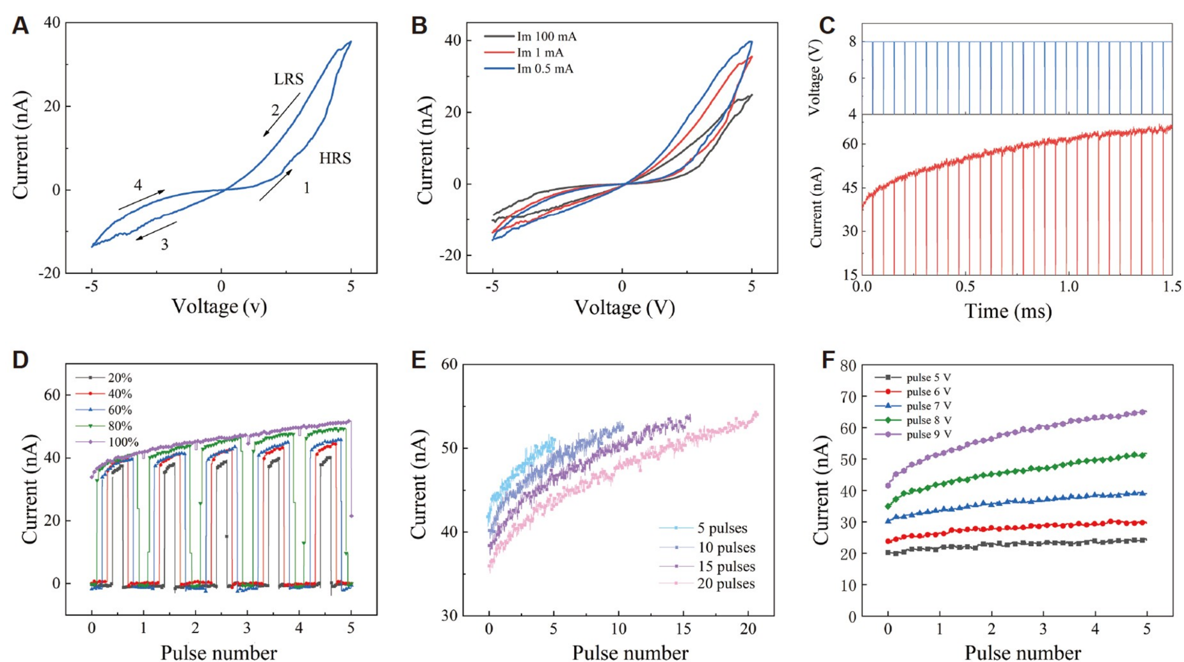

Figure 3 Electrical performance of a Pt/GO/rGO memristor. (A) Resistive switching behaviors of Pt/GO/rGO memristor; (B) resistive switching behavior of the Pt/GO/rGO memristor under different current compliance; (C) pulse switching characteristics. Electrical pulses (8 V, 50 μs) with an interval of 1 μs were used. (D) Modulation of switching characteristics by different pulse duty cycles; (E) modulation of switching characteristics by different pulse numbers; (F) modulation of switching characteristics by different pulse amplitudes.

In the memory devices with GO as the insulator media and metal as the electrode, the resistive switching is usually attributed to the oxygen migration, and/or the metal filament arising from the diffusion of the top metal electrode into the GO film during the evaporation process [41,42]. In the current work, since rGO electrodes were used and it is difficult to form Pt conductive filaments in memristors considering its chemical inertness, the metal filament cannot be used to explain the resistive switching. According to the existing principles of different types of memristor analysis, the charge trapping and detrapping on the oxygen-containing groups of GO sheets might be responsible for the switching effect [43]. The details of the electrical transition, carrier-transport mechanism, and the effect of an rGO electrode in this memory device are under investigation. It can be observed that the lateral device exhibited a reversible hysteresis during the voltage sweep, which is useful for simulating synaptic properties similar to biological synapses. We intend to attribute the observed resistive switching to the desorption/absorption of oxygen-containing groups on the GO sheets. A multilevel switching event can also be achieved by varying the compliance current (Figure 3B). The conductivity of the device increases as the compliant current increases. This may be due to the effect of compliance current on the desorption/absorption of oxygen-containing groups.

Most research on memristor devices focused on achieving gradually changed analogue behavior like human synapses [44]. In order to verify that the Pt/GO/rGO memristors have the basic properties of emulating synapse, continuous positive and negative pulse voltage scanning is applied to the device. The Pt/GO/rGO memristor displays a corresponding decreasing or increasing current depending on the polarity of the applied voltage. The plasticity of synaptic transmission refers to the increase or decrease of synaptic transmission efficiency caused by repeated activities of synapses, mainly manifested in short-term memory (STM). STM plays a vital role in the information transmission and processing of neural networks. The device exhibits a continuous increase in behavior in conductance, which is STM of synapses through continuous training (Figure 3C). To further investigate the properties of gradual change in conductance, pulses with different characteristics are attached to the devices. Figure 3D shows the increase in the conductance of devices as the increase in pulse duty cycles under the fixed amplitude (8 V). A strong dependency of conductance increases between stimulation pulse duty cycles can be observed in Figure 3D, showing a larger conductance increase with increasing pulse width in synapse potentiation process. Figure 3E shows the change of the conductance of the device under different numbers of pulses (5–20 pulses). It can be seen that when the number of pulses of the same polarity is more, the conductance of the device will increase continuously. The update of synaptic weights can be achieved by changing the number of pulse excitations, which is also known as the learning process. Furthermore, Figure 3F shows the conductance after the same 5 pulses, the conductance of cells increases with different amplitudes (5–9 V). A larger amplitude will lead to a higher beginning and ultimate conductance. Overall, the conductance of synapses can be well tuned by the amplitude, pulse duty cycles and the number of pulses, which are favorable to obtain a synapse weight update with a suitable stimulation pulse and improve the fault tolerance in neuromorphic computing.

Table 1 [45–49] shows the comparison of energy consumption between the Pt/GO/rGO memristor in this work and other reported lateral devices. The device has a lower energy consumption (200 nW) and a nano-ampere current, which is much lower than the energy consumption of the same type of lateral structure memristor. It is believed that the low power consumption of the device is governed by a mechanism of oxygen migration. Absorption and desorption of oxygen functional groups could induce resistive switching in the GO film [50]. This is reasonable because Pt is noble and inert metal with low reactivity with GO [51].

Table 1 Comparison of the device characteristics of the lateral structure memristor devices

Structure	SET voltage (V)	Operation current (A)	Power (W)	Ref.
Au-MoS_2-Au	80	10^{-4}	8×10^{-3}	[45]
Ti-TaS_2-Ti	3	10^{-3}	3×10^{-3}	[46]
Au-MoS_2-Au	3	10^{-5}	3×10^{-5}	[47]
Ti/Au-MoS_2-Ti/Au	15	10^{-4}	15×10^{-4}	[48]
Au/Ti-MoS_2-Ti/Au	6	10^{-3}	6×10^{-3}	[49]
Pt-GO-rGO	5	4×10^{-8}	2×10^{-7}	This work

Therefore, the device does not need a large SET voltage to complete the forming process. GO is associated with various oxygen groups, such as carboxyl, hydroxyl, and epoxide, with their oxygen ions usually contributing to form the conduction filament [52]. We anticipate that the oxygen defects are enhanced by the RGO electrode [53], so that absorption and desorption of oxygen functional groups in GO can be reproducibly achieved to achieve bipolar switching properties.

The desorption and absorption of the oxygen-related groups on the GO sheets correspond to the on and off states, respectively [54]. A sudden current increase that switches the device to LRS is probably related to the movement of oxygen ions from GO towards the rGO surface, which contains large amounts of oxygen vacancies compared to the bulk region [55]. Therefore, the device can be kept in a lower power consumption state after SET. And the resistance of the rGO electrode is decreased by reducing the oxygen vacancy concentration, inducing the reset and transition back to the HRS. Electrical pulses can cyclically induce an HRS to LRS transition [56]. The realization of ultra-low energy consumption is also of great significance to the development of NC systems.

To illustrate the potential application of memristors in NC, a digital recognition function demonstration was carried out. A 5×1 memristor array is used to demonstrate the role of the reservoir in the RC system. The structure diagram and physical diagram of the memristor array are shown in Figure 4. A recurrent neural network (RNN) is widely used to process various dynamic sequence events [57]. RC is a new type of RNN, which is mainly divided into two parts: the reservoir and the readout layer. The reservoir is connected to the input terminal and its connection structure is fixed. The structure of the reservoir will dynamically change with the input signal over time, and the input signal will be mapped to the high-dimensional state through nonlinear mode. The function of the readout layer is to process the signals obtained in the reservoir and identify the corresponding numbers.

The entire RC system only involves the training of the single layer weights in the readout layer, which greatly reduces the training cost and solves the problem of the slow calculation process of a fully connected neural network (FNN). There are several requirements for a physical reservoir to efficiently solve computational tasks. First, it should nonlinearly transform the input signal into a high-dimensional state space in which the signal is represented. Second, the status of the reservoir is time series, which is determined by the current input and the input of a certain period in the past. So the characteristics of STM are essential to the reservoir [58]. Additionally, the results of RC computations must be reproducible and robust against noise. For this, the reservoir should exhibit sufficiently different dynamical responses to inputs belonging to different classes. At the same time, the reservoir should not be too sensitive, so that similar inputs are classified into the same class [59].

Memristive systems and devices are capable of exhibiting nonlinear dynamics and responding to inputs in a

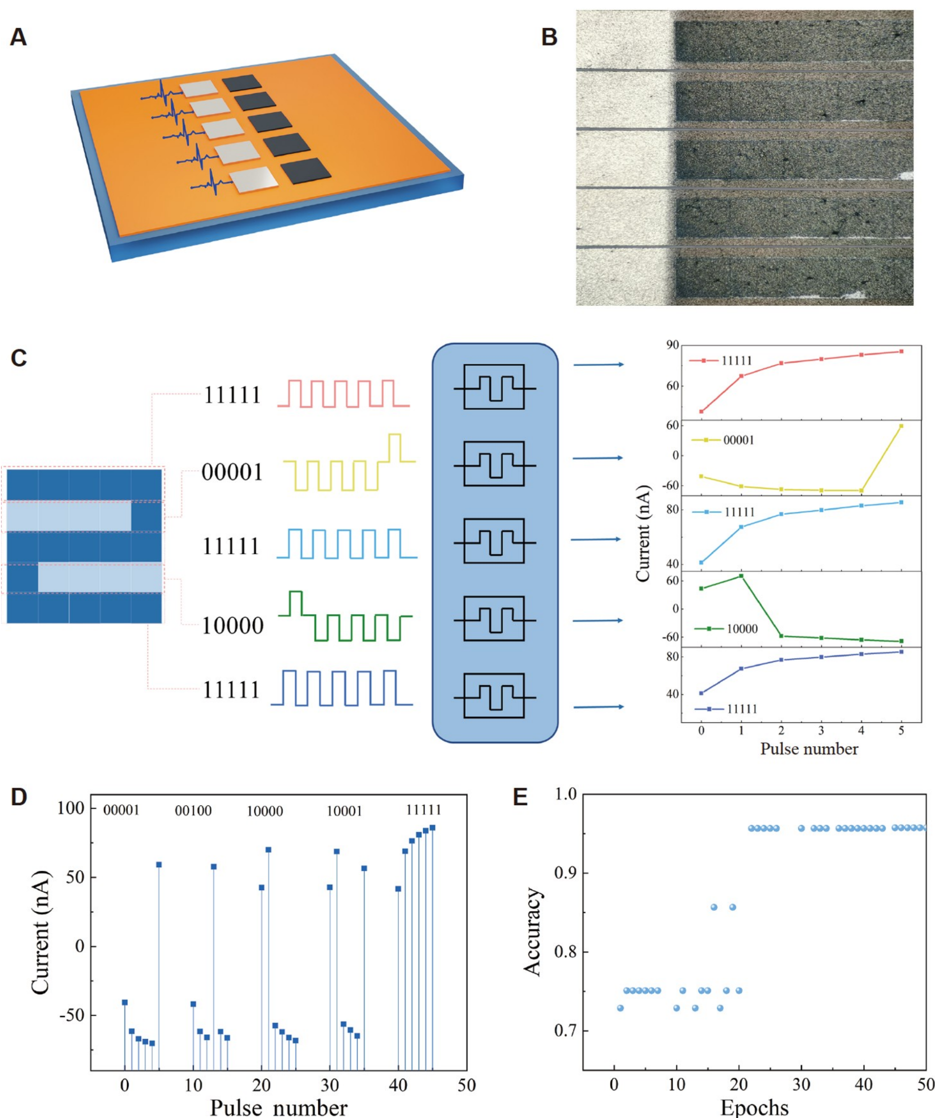

Figure 4 Application of Pt/GO/rGO memristor array in reservior computing (RC). (A) Demonstration diagram of memristor array. (B) An image of memristor array under microscope. (C) Schematic of the operation of RC based on Pt/GO/rGO memristors for classifying numbers. (D) Experimental read-current responses of a memristor by several electrical input signals. The amplitude and width of the read pulses are correspondingly 8 V and 500 μs. (E) The evolution of the classification accuracy rates using standard batch gradient descent within 50 epochs.

history-dependent manner. By exploiting these favorable properties for a dynamic reservoir, we proposed reservoirs based on memristive systems. The nonlinearity and the synaptic plasticity of memristors make the memristor array a favorable candidate for hardware simulation of the reservoir [60]. An integrated memristor array was fabricated to demonstrate the dynamic reservoir (Figure 4A) and Figure 4B shows an optical image of the memristor array under an optical microscope.

The input signals are pulse voltage sequences of a simple digital image, and the corresponding current states are collected by an integrated memristor array. The memristor array is connected to a readout layer for network training that recognizes numbers by training current states of the input image. In particular, the input 5×5 image has 25 pixels and is composed of light blue pixels (−1) and dark blue pixels (1). Divide the image

into 5 rows, each row has 5 continuous pixels. We input them into the memristor matrix as the pulse voltage of 5-time frames. The current states of the five integrated memristors are used to characterize the state of the reservoir (Figure 4C). A device in the array is chosen randomly to measure its response to 5 different pulse streams. For different inputs, the read currents of all devices are highly differentiated (Figure 4D). Due to the STM of the device, when multiple pulses are applied in a short interval, the conductance of the device will continue to increase and the reverse stimulation will cause the memristor state to decay to the initial state. Thus, the current state of each memristor in the memristor array after pulse stimulation will represent the information in each line of the original image. For 10-digit numbers 0–9, the memristor has 10 different pulse curves that can be used to separate these 10 different input numbers (Figure S5, Supporting Information).

The conductivity of the memristor which represents the state of reservoir can realize the function of digital recognition by training the readout layer. We input all the sequences generated in the digital image into the memristor array to obtain different and easily distinguishable conductance states. At the same time, the same timing pulse was input to multiple memristors prepared under the same conditions, and the highly consistent conductivity variation trend was obtained, which further verified the high uniformity of the device (Figure S6, Supporting Information). The readout layer is a 5×10 single-layer neural network, which is linearly weighted between inputs and weights and trained by activation functions (see Experimental Section). The final conductivity value in memristor array is used as input and 10 values (0–9) representing the predicted number of the image are used as output. After 50 training iterations, the recognition accuracy of the RC system for the original image can reach 95.74% (Figure 4E).

For FNN, even a single-layer 25×10 network with the same number recognition function needs 25 inputs and 250 weights to be trained, which is far more complex than the readout layer of RC system. The digital pictures identified in the experiment are standard digital pictures that are considered to be designed, so only a memristor array composed of five memristive devices can achieve high-accuracy digital identification. For complex pictures of handwritten numbers, pulse sequence input can also be performed by dividing the different pixels in the picture, but the number of devices in the corresponding memristor array should be correspondingly increased according to the number of rows of the picture.

CONCLUSION

In summary, we fabricated a Pt/GO/rGO lateral structure memristor based on DLW technology. DLW technology is a fast, inexpensive and flexible fabrication of graphene, which has a wide application prospect. Using DLW, graphene can be modified easily, quickly, and in large areas. Due to the characteristics of GO as an active layer, the device exhibits ultra-low power consumption (200 nW) compared to memristors with the same lateral structure. The device successfully simulates the characteristics of biological synapses (STM) and realizes the change of synaptic weight by adjusting parameters such as pulse number, amplitude, and duty cycle. We also used a 5×1 memristor array as the reservoir part of RC system, combined with a 5×10 single-layer neural network to achieve 95.74% accuracy in digit recognition. It further verifies the advantages of memristors in neural network computing applications. The realization of memristors and their arrays based on DLW technology is flexible, highly integrated and low-power which can be well applied to wearable devices, NC hardware platforms, and the integration of other carbon-based devices in the future.

EXPERIMENTAL SECTION

Device preparation. The precursor material used for memristor preparation is GO colloid (4 mg mL^{-1}, from Sigma-Aldrich Corp). The GO solution was diluted to a concentration of 1 mg mL^{-1} and ultrasonic treatment was performed for 1 h to obtain a uniformly mixed suspension. A 25 mm×25 mm×0.7 mm fused silica plate was cleaned in acetone with the aid of ultrasound. The glass substrate becomes hydrophilic after treatment with concentrated sulfuric acid and hydrogen peroxide. Finally, the 500 μL GO solution was dripped onto the glass substrate by instillation method, and a GO film with a thickness of 869 nm was obtained after drying in the air at room temperature.

The Pt electrode is made by using a magnetron sputtering device (JS-3, TM) with a mask to vapor-deposit a metal electrode of 3 mm×5 mm×50 nm on the surface of the prepared GO film. A Pt/GO/rGO lateral structure memristor is obtained by writing an rGO electrode with a commercial DLW system (Nanoscribe, Photonic Professional (GT) with laser peak power between 16 mW and 56 mW, 80 MHz repetition rate, laser scan speed 10 mm s^{-1}, wavelength of laser 780 nm, a 0.5-NA objective) near the Pt electrode. The resulting size of the rGO electrode is 1800 μm×300 μm, and the width of GO active layer between the two electrodes is 60 μm.

Characterization method. Raman spectra were obtained with a confocal Raman system (WITEC Alpha 300RA) under 532 nm laser excitation with a 5% attenuation and acquisition time of 10 s. The morphologies of the sample were observed using SEM (Zeiss Gemini 300) and AFM (Bruker Dimension Icon). XPS was performed with ThermoFisher (ESCALAB 250Xi, USA). Electrical characterization was conducted with a Keithley 4200 semiconductor parameter analyzer (Tektronix, USA) and a probe station (Cascade).

Network training. Here, different pulse definitions are made for different color pixels. The dark blue pixel corresponds to a voltage pulse with an amplitude of 8 V and a pulse width of 500 μs; the light blue pixel corresponds to a voltage pulse with an amplitude of −8 V and a pulse width of 500 μs. The interval between pulse voltages is 1 μs. We test pulse sequences of different numbers while randomly adding different noise pixels to the image. The device exhibits ns-level switching speeds with an average pulse power consumption of 400 nA. Here 500 output current response values were tested for each digit. A total of 5000 memristor arrays' current response values were measured. The 5000 datasets are randomly divided into 80% as the training dataset and 20% as the test dataset as the input of the readout layer network to train a 5×10 single-layer network.

We used a 5×1 memristor array as the reservoir part of RC system, combined with a 5×10 single-layer neural network in Python software. For a 5×10 single-layer perceptron, the conductance states of the five memristor matrices after the last time pulse flows through the reserve pool are used as the input of the readout layer. Use softmax as the activation function. The classification cross-entropy loss is minimized by gradient descent in a mini-batch using the Adam optimizer (learning rate=0.09). For support vector machines, select the linear kernel option for linear classification.

Data availability

All data generated during this study are included in this published article.

Funding

This work was supported by the Science and Technology Commission of Shanghai Municipality (21DZ1100500), the Shanghai Municipal Science and Technology Major Project, the Shanghai Frontiers Science Center Program (2021-2025 No. 20), the Zhangjiang National Innovation Demonstration Zone (ZJ2019-ZD-005), the National Key Research and Development Program of China (2021YFB2802000), the National Natural Science Foundation of China (61975123 and 62105206), and China Postdoctoral Science Foundation (2021M692137).

Author contributions

M. Chen, Dr. Z. Wan, H. Dong and Dr. Q. Chen conceived and wrote the manuscript. Prof. Q. Zhang and Prof. M. Gu initiated and supervised the project. All authors read and approved the submission of the manuscript.

Conflict of interest

The authors declare that they have no conflict of interest.

Supplementary information

The supporting information is available online at https://doi.org/10.1360/nso/20220020. The supporting materials are published as submitted, without typesetting or editing. The responsibility for scientific accuracy and content remains entirely with the authors.

References

1 Pedretti G, Milo V, Ambrogio S, *et al.* Memristive neural network for on-line learning and tracking with brain-inspired spike timing dependent plasticity. *Sci Rep* 2017; **7**: 5288.

2 Ielmini D, Wong HSP. In-memory computing with resistive switching devices. *Nat Electron* 2020; **1**: 333–343.

3 Zhang C, Zhou H, Chen S, *et al.* Recent progress on 2D materials-based artificial synapses. *Crit Rev Solid State Mater Sci* 2021; https://doi/org/10.1080/10408436.2021.1935212.

4 Porro S, Accornero E, Pirri CF, *et al.* Memristive devices based on graphene oxide. *Carbon* 2015; **85**: 383–396.

5 Jo SH, Chang T, Ebong I, *et al.* Nanoscale memristor device as synapse in neuromorphic systems. *Nano Lett* 2010; **10**: 1297–1301.

6 Schranghamer TF, Oberoi A, Das S. Graphene memristive synapses for high precision neuromorphic computing. *Nat Commun* 2020; **11**: 1.

7 Sharbati MT, Du Y, Torres J, *et al.* Low-power, electrochemically tunable graphene synapses for neuromorphic computing. *Adv Mater* 2018; **30**: 1802353.

8 Pickett MD, Medeiros-Ribeiro G, Williams RS. A scalable neuristor built with Mott memristors. *Nat Mater* 2013; **12**: 114–117.

9 Goi E, Zhang Q, Chen X, *et al.* Perspective on photonic memristive neuromorphic computing. *PhotoniX* 2020; **1**: 3.

10 Wang Z, Joshi S, Savel'ev S, *et al.* Fully memristive neural networks for pattern classification with unsupervised learning. *Nat Electron* 2018; **1**: 137–145.

11 Strukov DB, Snider GS, Stewart DR, *et al.* The missing memristor found. *Nature* 2008; **453**: 80–83.

12 Hui F, Grustan-Gutierrez E, Long S, *et al.* Graphene and related materials for resistive random access memories. *Adv Electron Mater* 2017; **3**: 1600195.

13 Ji Y, Cho B, Song S, *et al.* Stable switching characteristics of organic nonvolatile memory on a bent flexible substrate. *Adv Mater* 2010; **22**: 3071–3075.

14 Wang H, Zou C, Zhou L, *et al.* Resistive switching characteristics of thin NiO film based flexible nonvolatile memory devices. *MicroElectron Eng* 2012; **91**: 144–146.

15 Liang J, Chen Y, Xu Y, *et al.* Toward all-carbon electronics: Fabrication of graphene-based flexible electronic circuits and memory cards using maskless laser direct writing. *ACS Appl Mater Interfaces* 2010; **2**: 3310–3317.
16 Yang YC, Pan F, Liu Q, *et al.* Fully room-temperature-fabricated nonvolatile resistive memory for ultrafast and high-density memory application. *Nano Lett* 2009; **9**: 1636–1643.
17 Long S, Perniola L, Cagli C, *et al.* Voltage and power-controlled regimes in the progressive unipolar RESET transition of HfO_2-based RRAM. *Sci Rep* 2013; **3**: 2929.
18 Yu M, Cai Y, Wang Z, *et al.* Novel vertical 3D structure of TaO_x-based RRAM with self-localized switching region by sidewall electrode oxidation. *Sci Rep* 2016; **6**: 21020.
19 Sarkar B, Lee B, Misra V. Understanding the gradual reset in $Pt/Al_2O_3/Ni$ RRAM for synaptic applications. *Semicond Sci Technol* 2015; **30**: 105014.
20 Shim JH, Hu Q, Park MR, *et al.* Resistive switching characteristics of TiO_2 thin films with different electrodes. *J Korean Phys Soc* 2015; **67**: 936–940.
21 Sangwan VK, Jariwala D, Kim IS, *et al.* Gate-tunable memristive phenomena mediated by grain boundaries in single-layer MoS_2. *Nat Nanotech* 2015; **10**: 403–406.
22 Wu W, Wu H, Gao B, *et al.* Suppress variations of analog resistive memory for neuromorphic computing by localizing V_o formation. *J Appl Phys* 2018; **124**: 152108.
23 Liu J, Yin Z, Cao X, *et al.* Bulk heterojunction polymer memory devices with reduced graphene oxide as electrodes. *ACS Nano* 2010; **4**: 3987–3992.
24 Geim AK, Novoselov KS. The rise of graphene. *Nat Mater* 2007; **6**: 183–191.
25 Rehman MM, Rehman HMMU, Gul JZ, *et al.* Decade of 2D-materials-based RRAM devices: A review. *Sci Tech Adv Mater* 2020; **21**: 147–186.
26 Wan Z, Streed EW, Lobino M, *et al.* Laser-reduced graphene: Synthesis, properties, and applications. *Adv Mater Technol* 2018; **3**: 1700315.
27 Chen Y, Zhang B, Liu G, *et al.* Graphene and its derivatives: Switching on and off. *Chem Soc Rev* 2012; **41**: 4688–4707.
28 Tian H, Chen HY, Ren TL, *et al.* Cost-effective, transfer-free, flexible resistive random access memory using laser-scribed reduced graphene oxide patterning technology. *Nano Lett* 2014; **14**: 3214–3219.
29 Wan Z, Umer M, Lobino M, *et al.* Laser induced self-N-doped porous graphene as an electrochemical biosensor for femtomolar miRNA detection. *Carbon* 2020; **163**: 385–394.
30 Yang C, Huang Y, Cheng H, *et al.* Rollable, stretchable, and reconfigurable graphene hygroelectric generators. *Adv Mater* 2019; **31**: 1805705.
31 Zhao F, Cheng H, Hu Y, *et al.* Functionalized graphitic carbon nitride for metal-free, flexible and rewritable nonvolatile memory device via direct laser-writing. *Sci Rep* 2015; **4**: 5882.
32 Bhaumik A, Narayan J. Wafer scale integration of reduced graphene oxide by novel laser processing at room temperature in air. *J Appl Phys* 2016; **120**: 105304.
33 Cui P, Seo S, Lee J, *et al.* Nonvolatile memory device using gold nanoparticles covalently bound to reduced graphene oxide. *ACS Nano* 2011; **5**: 6826–6833.
34 Wan Z, Wang S, Haylock B, *et al.* Tuning the sub-processes in laser reduction of graphene oxide by adjusting the power and scanning speed of laser. *Carbon* 2019; **141**: 83–91.
35 Zhang Y, Guo L, Wei S, *et al.* Direct imprinting of microcircuits on graphene oxides film by femtosecond laser reduction. *Nano Today* 2010; **5**: 15–20.
36 Zhang YL, Guo L, Xia H, *et al.* Photoreduction of graphene oxides: Methods, properties, and applications. *Adv Opt Mater* 2014; **2**: 10–28.
37 Chen HY, Han D, Tian Y, *et al.* Mask-free and programmable patterning of graphene by ultrafast laser direct writing. *Chem Phys* 2014; **430**: 13–17.
38 Romero FJ, Toral-Lopez A, Ohata A, *et al.* Laser-fabricated reduced graphene oxide memristors. *Nanomaterials* 2019; **9**: 897.

39 Strong V, Dubin S, El-Kady MF, *et al.* Patterning and electronic tuning of laser scribed graphene for flexible all-carbon devices. *ACS Nano* 2012; **6**: 1395–1403.

40 Belete M, Kataria S, Turfanda A, *et al.* Nonvolatile resistive switching in nanocrystalline molybdenum disulfide with ion-based plasticity. *Adv Electron Mater* 2020; **6**: 1900892.

41 He CL, Zhuge F, Zhou XF, *et al.* Nonvolatile resistive switching in graphene oxide thin films. *Appl Phys Lett* 2009; **95**: 232101.

42 Zhuge F, Hu B, He C, *et al.* Mechanism of nonvolatile resistive switching in graphene oxide thin films. *Carbon* 2011; **49**: 3796–3802.

43 Hu B, Quhe R, Chen C, *et al.* Electrically controlled electron transfer and resistance switching in reduced graphene oxide noncovalently functionalized with thionine. *J Mater Chem* 2012; **22**: 16422–16430.

44 Liang A, Zhang J, Wang F, *et al.* Transparent HfO_x-based memristor with robust flexibility and synapse characteristics by interfacial control of oxygen vacancies movement. *Nanotechnology* 2021; **32**: 145202.

45 Sangwan VK, Lee HS, Bergeron H, *et al.* Multi-terminal memtransistors from polycrystalline monolayer molybdenum disulfide. *Nature* 2018; **554**: 500–504.

46 Yoshida M, Suzuki R, Zhang Y, *et al.* Memristive phase switching in two-dimensional 1T-TaS_2 crystals. *Sci Adv* 2015; **1**: 1–7.

47 Zhu X, Li D, Liang X, *et al.* Ionic modulation and ionic coupling effects in MoS_2 devices for neuromorphic computing. *Nat Mater* 2019; **18**: 141–148.

48 Li D, Wu B, Zhu X, *et al.* MoS_2 memristors exhibiting variable switching characteristics toward biorealistic synaptic emulation. *ACS Nano* 2018; **12**: 9240–9252.

49 Wang L, Liao W, Wong SL, *et al.* Artificial synapses based on multiterminal memtransistors for neuromorphic application. *Adv Funct Mater* 2019; **29**: 1901106.

50 Shi K, Wang Z, Xu H, *et al.* Complementary resistive switching observed in graphene oxide-based memory device. *IEEE Electron Device Lett* 2018; **39**: 488–491.

51 Kim I, Siddik M, Shin J, *et al.* Low temperature solution-processed graphene oxide/$Pr_{0.7}Ca_{0.3}MnO_3$ based resistive-memory device. *Appl Phys Lett* 2011; **99**: 042101.

52 Gao S, Yi X, Shang J, *et al.* Organic and hybrid resistive switching materials and devices. *Chem Soc Rev* 2019; **48**: 1531–1565.

53 Jetty P, Sahu DP, Jammalamadaka S. Analog resistive switching in reduced graphene oxide and chitosan-based bio-resistive random access memory device for neuromorphic computing applications. *Physica Rapid Res Ltrs* 2022; **16**: 2100465.

54 Wang LH, Yang W, Sun QQ, *et al.* The mechanism of the asymmetric SET and RESET speed of graphene oxide based flexible resistive switching memories. *Appl Phys Lett* 2012; **100**: 063509.

55 Mkhoyan KA, Contryman AW, Silcox J, *et al.* Atomic and electronic structure of graphene-oxide. *Nano Lett* 2009; **9**: 1058–1063.

56 Saini P, Singh M, Thakur J, *et al.* Probing the mechanism for bipolar resistive switching in annealed graphene oxide thin films. *ACS Appl Mater Interfaces* 2018; **10**: 6521–6530.

57 Du C, Cai F, Zidan MA, *et al.* Reservoir computing using dynamic memristors for temporal information processing. *Nat Commun* 2017; **8**: 2204.

58 Sun L, Wang Z, Jiang J, *et al.* In-sensor reservoir computing for language learning via two-dimensional memristors. *Sci Adv* 2021; **7**: eabg1455.

59 Appeltant L, Soriano MC, Van der Sande G, *et al.* Information processing using a single dynamical node as complex system. *Nat Commun* 2011; **2**: 1–6.

60 Tanaka G, Yamane T, Héroux JB, *et al.* Recent advances in physical reservoir computing: A review. *Neural Networks* 2019; **115**: 100–123.